J Appl Electrochem (2010) 40:265–275
DOI 10.1007/s10800-009-9970-7

ORIGINAL PAPER

Chemical composition and electrochemical activity of some chemically synthesized γ-MnO_2

Hemant Malankar · S. S. Umare · K. Singh

Received: 12 September 2008 / Accepted: 17 August 2009 / Published online: 3 September 2009

Abstract A series of γ-MnO_2 with Mn^{4+} cation vacancy fraction $1.5 < x < 2.3$ was prepared via chemical synthesis. X-ray diffraction (XRD) revealed high degree of microtwinning ($T_w > 70\%$) and de Wolff disorder ($0.32 < P_r < 0.35$) in the prepared samples. Thermal analysis showed four-stage decomposition corresponding to the removal of physical water, chemisorbed water, formation of Mn_2O_3 and Mn_3O_4, respectively. The chemical composition and physical properties of the prepared samples were expressed in terms of Ruetschi's cation vacancy model for MnO_2. The discharge behavior in 9 M KOH was governed by homogeneous solid-state reduction wherein protons and electrons were simultaneously inserted into MnO_2 lattice. Their electrochemical behavior was also studied by performing cyclic voltammetry in 9 M KOH. An attempt was made to correlate obtained energy density as a function of proton transfer rate during the discharge process.

Keywords γ-MnO_2 · Mn^{4+} cation vacancy · Microtwinning · Chemical composition · 9 M KOH

1 Introduction

γ-MnO_2 is the most common positive electrode material used in dry cell due to (i) its ability to sustain relatively high discharge rates for prolonged periods of time; (ii) an abundance of the raw materials necessary for synthesis; and (iii) the low cost of production [1]. Structurally, it belongs to a large family of closely related compounds whose physical and chemical properties can be varied significantly by changing the preparative conditions [2]. Ever since the discovery of chemically synthesized γ-MnO_2 (Glemser; 1939), its structure and chemical composition have become major areas of research. They are mainly known for a great variety of X-ray diffraction (XRD) patterns, which reveal structural disorder due to chemical defects induced during the synthesis [3]. In 1959, de Wolff [4] proposed that the great diversity in XRD patterns of γ/ε-MD is produced by a regular intergrowth of pyrolusite structural blocks in an initial ramsdellite network. de Wolff model successfully accounted for many features in the XRD patterns of chemically synthesized manganese dioxides (CMD). However, it could not explain those of synthetic forms prepared by electrodeposition (EMD), which typically contain 6 broad lines, compared to the 14 in synthetic ramsdellite. Pannetier [5] explained such broadening of specific reflections, as well as the occurrence of an apparently hexagonal structure on the basis of twinning of the orthorhombic ramsdellite lattice on the 021 and/or 061 planes. A new structural model [6] allows the diffraction patterns of the γ-MnO_2 to be analyzed by considering two types of defects: P_r, intergrowth of pyrolusite structural blocks in the ramsdellite network (de Wolff disorder), and T_w, microtwinning of this interspersed structure. These defects influence the electrochemical properties of γ-MnO_2 to certain extent [7].

Besides the structural disorder, γ-MnO_2 is known for non-stoichiometric compositions MnO_x wherein $x < 2$ [6] and always contains water or, protonic species [8]. Based on their theory, Coeffier and Brenet [9] formulated the following composition for γ-MnO_2:

H. Malankar (✉) · S. S. Umare
Department of Chemistry, Visvesvaraya National Institute of Technology, Nagpur 440010, India
e-mail: hemant.malankar@gmail.com

K. Singh
Sant Gadge Baba Amaravati University, Amaravati 444602, India

$(MnO_2)_{2n-3}(MnOOH)_{4-2n}(H_2O)_m$

where n and m are composition parameters determined by classical chemical analysis. A major step in the chemical understanding of γ-MnO_2 was achieved by Ruetschi [10], when he demonstrated that chemical composition, density, and several other parameters could be explained by assuming non-stoichiometry based on Mn^{4+} cation vacancy model. His theory yielded following formulation:

$Mn_{(1-x-y)}{}^{4+}Mn_y{}^{3+}\square_x O_{(2-4x-y)}(OH)_{4x+y}$

where $\square$ denotes Mn^{4+} cation vacancy, x is the fraction of Mn^{4+} missing from the MnO_2 lattice resulting in Mn vacancies, and y is the fraction of Mn^{4+} replaced by Mn^{3+}. This model gives a good account of itself in predicting and correlating some of the crucial physical properties such as structural/combined water, density, electronic conductivity, proton transfer rate, and electrochemical activity with Mn^{4+} vacancies [11]. However, except few workers [11–14], the model has been less attempted for explaining electrochemical activity of γ-MnO_2.

In view of this situation, a series of samples belonging to γ-MnO_2 family with different cation vacancy fraction have been synthesized by chemical method. A structural description of XRD patterns on the basis of de Wolff disorder and microtwinning is presented. Physical properties and chemical composition are explained in light of Ruetschi's model. Their electrochemical behavior has been studied by recording discharge profile and cyclic voltammetry in 9 M KOH.

2 Experimental

2.1 Materials

Industrial grade $MnSO_4$ (Mn content = 33%) was procured from Navrang Chemicals Industries, Nagpur, India. Liquor ammonia (30%) and HNO_3, HCl, H_2SO_4, EDTA, and oxalic acid, were of MERCK (AR) grade. Thymolphthalein complexone, KOH, graphite were of Sigma-aldrich (AR) grade.

2.2 Synthesis

MnO_2 has been synthesized by O_2-oxidation of industrial grade $MnSO_4$ in the presence of NH_4OH. One hundred grams of $MnSO_4$ was dissolved in 400 ml of double-distilled water. The resultant solution was stirred for 30 min at room temperature. Insoluble impurities were removed by filtration. Liquor ammonia was added into the filtrate till pH of mixture is 10, to precipitate manganese hydroxide. The $Mn(OH)_2$ precipitate was filtered and washed with the distilled water till the filtrate showed pH 7. The obtained precipitate was suspended in 200 ml water and oxygen was passed through suspension for 18 h at the rate 4 L min^{-1} at different temperatures viz. room temperature (27 °C), 40, 60, and 80 °C. It was further subjected to disproportionation in conc. nitric acid. The MnO_2 obtained by O_2-oxidation at different temperature(s) i.e. RT, 40, 60, and 80 °C are, henceforth designated by the acronyms MDO-O-RT, MDO-O-40, MDO-O-60, and MDO-O-80, respectively. All the samples were dried at 110 °C for 1 h and cooled in a dessicator.

2.3 Structural characterization

The XRD patterns of the synthesized samples were recorded using PANalytical diffractometer (Philips, Holland) with Cu Kα radiation. The scans were recorded in 2θ range 15–80°. FTIR for the prepared MnO_2 samples were recorded on Shimadzu spectrophotometer in the frequency range of 400–4,600 cm^{-1}. The morphology of each sample were examined with a JEOL scanning electron microscope.

2.4 Thermal analysis

Differential thermal analysis (DTA) and thermogravimetry (TG) was carried out in inert atmosphere using Perkin Elmer Diamond Instrument. The temperature range was from 25 to 1,000 °C with heating rate of 5 °C min^{-1}.

2.5 Chemical analysis

Total Mn content was estimated by complexometric titration against EDTA [15]. Available oxygen in terms of % MnO_2 was determined by redox titration against standardized $KMnO_4$ [16].

2.6 Electrochemical activity

The electrochemical activity of the prepared samples was evaluated by recording discharge profile in 9 M KOH electrolyte solution at constant current of 1 mA and constant resistance of 100 Ω at 27 °C (room temperature). The experimental cell consisted of a zinc anode strip (50 × 10 mm) and the cathode consisting of 0.1 g of the synthesized MnO_2 dispersed in 0.4 g of graphite powder wetted with 0.5 ml of electrolyte (9 M KOH solution) and carboxymethyl cellulose binder. For discharge profile at 100 Ω, cathode mixture consisted of 0.5 g MnO_2 dispersed in 0.5 g graphite powder. The cathodic ingredients were pressed in a cylindrical Teflon container (50 mm height and 20 mm diameter) with a spiral platinum wire at the bottom for electrical contact at a pressure of 100 kg cm^{-2} (Fig. 1). A circular, perforated, Teflon disc was placed over

the compressed mixture for ionic transfer and to avoid diffusion of cathodic mixture into the electrolyte media. The cell was activated with 10 ml of electrolyte. The total cell assembly was allowed to equilibrate for 1 h at its open-circuit potential before measurement of continuous discharge till cutoff voltage 0.7 V (for 1 mA 0.1 g^{-1}) and 0.6 V (for 100 Ω 0.5 g^{-1}), respectively.

2.7 Cyclic voltammetry

Cyclic voltammetry of MDO-O-80 was carried out with a three-electrode setup comprising the MnO_2-containing Platinum working electrode and a Hg/HgO/9 M KOH reference electrode and Platinum wire auxiliary electrodes. The electrochemical cell was controlled and data were collected by Autolab Potentiostat-Galvanostat using the cyclic voltammetry software option. Voltammogram were recorded between −800 and 400 mV at 2 mV s^{-1} in 9 M KOH solution. MnO_2-containing working electrode was prepared according to the procedure described elsewhere [17].

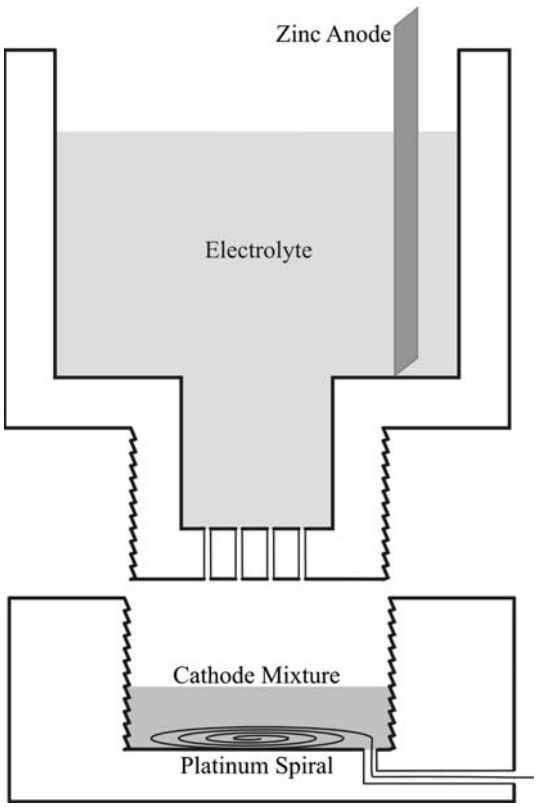

Fig. 1 Cross section of Teflon sample holder used for electrochemical activity

3 Results and discussion

3.1 X-ray diffraction analysis

Figure 2 presents XRD spectra of the prepared manganese dioxides. A typical poor quality γ-MnO_2 pattern with small number of broad and diffused peaks is observed. de Wolff [4] proposed a structural model for explaining XRD patterns of γ-MnO_2 on the basis of pyrolusite and ramsdellite structure. He described γ-MnO_2 as a random intergrowth of pyrolusite blocks in ramsdellite matrix. Using parameter P_r, i.e. de Wolff disorder, he successfully accounted for line shifts and broadening for lines 110 and 130. However, his model could not explain coalescence of lines h21/h40 and h02/h61, which are not affected by de Wolff disorder. Pannetier [5] explained it on the basis structural defect; microtwinning. They put forward a model [6] to analyze XRD patterns of γ-MnO_2 on the basis of P_r and T_w. The XRD patterns of MnO_2 prepared in this study are classified under "type III" γ-MnO_2 as per the model [6]. The samples show high microtwinning ($T_w >$ 70%), which results in coalescence of lines 221/240 and 061/002. Such patterns can no longer be indexed with an orthorhombic unit cell. Ignoring the presence of first line i.e. 110 in orthorhombic Pbnm indexing, they are to be indexed with a hexagonal cell with parameters $a_h = 2.78$ and $c_h = 4.43$ Å [6]. This type of cell was proposed by de Wolff et al. [18] for EMD samples called as ε-MnO_2. Recent reports [19, 20] describe ε-MnO_2 as a MnO_2 polymorph with hexagonal

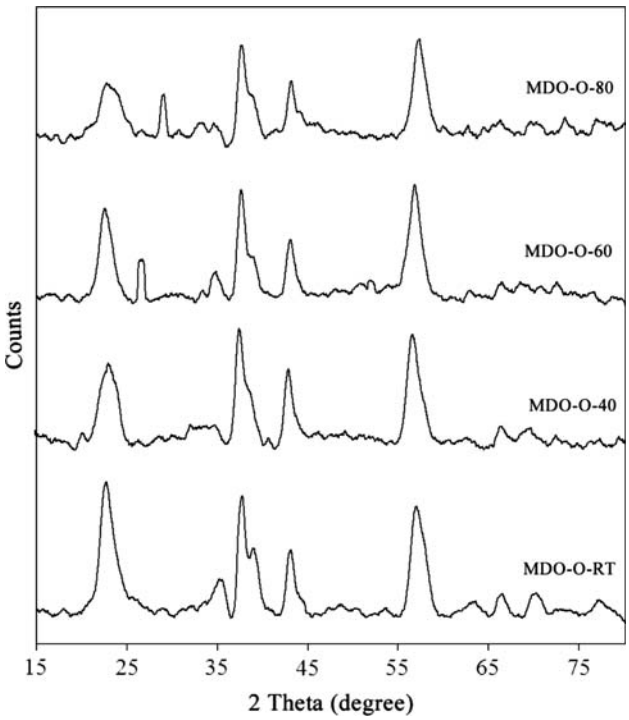

Fig. 2 XRD pattern of MnO_2 samples prepared at different temperatures

Table 1 Lattice, P_r and T_w parameters obtained from XRD measurements

Sample code	Crystal phase/type[a]	a (Å)	c (Å)	Cell volume (cm^3)	T_w (%)	P_r
MDO-O-RT	γ/III	2.804	4.443	30.255	>70	0.32
MDO-O-40	γ/III	2.799	4.482	30.412	>70	0.32
MDO-O-60	γ/III	2.797	4.447	30.135	>70	0.34
MDO-O-80	γ/III	2.798	4.461	30.252	>70	0.35
[6]	γ/III	2.78	4.43	–	>70	–
EMD [7]	γ/III	2.774	4.419	29.443	>70	0.37
EMD [7]	γ/III	2.775	4.424	29.510	>70	0.31
CMD [7]	γ/III	2.778	4.463	29.827	>70	0.44
[18]	γ	2.80	4.45	30.210	–	–

[a] represents the lattice parameter for hexagonal crystal symmetry of γ-MnO_2. The calculated lattice parameters 'a' and 'c' have been compared with those from reported literature values

symmetry with unit cells $a_h = 2.80$ and $c_h = 4.45$ Å, and space group $P6_3/mmc$. The structure is same as that of NiAs-type unit cell, with Mn^{4+} cations randomly occupying 50% of the octahedral positions of the hexagonal-close-packed (hcp) oxygen sublattice. Using Rietveld refinement, EMD has been described as comprising of ε-MnO_2, ramsdellite and pyrolusite phases. de Wolff disorder (P_r) is calculated from the displacement of peak 110 from orthorhombic position after correction for shift due to microtwinning. The obtained values are given in Table 1. The calculated lattice parameters (Table 1) are in good agreement with the values reported earlier [6, 7, 18].

3.2 FTIR analysis

Figure 3 presents FTIR spectra of the manganese dioxides prepared in this work. FTIR is a useful tool in locating the presence of hydroxyl groups and water molecules. All the prepared samples exhibit a well resolved peak at ~3,400 cm^{-1}, which indicates O–H stretching vibration [21–23]. A strong absorption band at ~1,620 cm^{-1} is associated with O–H bending vibration due to the water of crystallization [21]. The broad absorption band in the fingerprint region 600–400 cm^{-1} confirms the formation of γ-phase, whereas absorption band at 1,100 cm^{-1} is attributed to the presence of hydrogen bonding and/or MnO_2 stretching mode [13].

3.3 SEM

SEM images of synthesized MnO_2 samples are presented in Fig. 4. The particles are irregular and random in shape. Samples exhibit porous morphology with agglomerating tendency forming a cluster.

3.4 Thermal analysis

The thermogravimetric analysis of the prepared samples (Fig. 5) shows a typical γ-MnO_2 behavior with weight loss

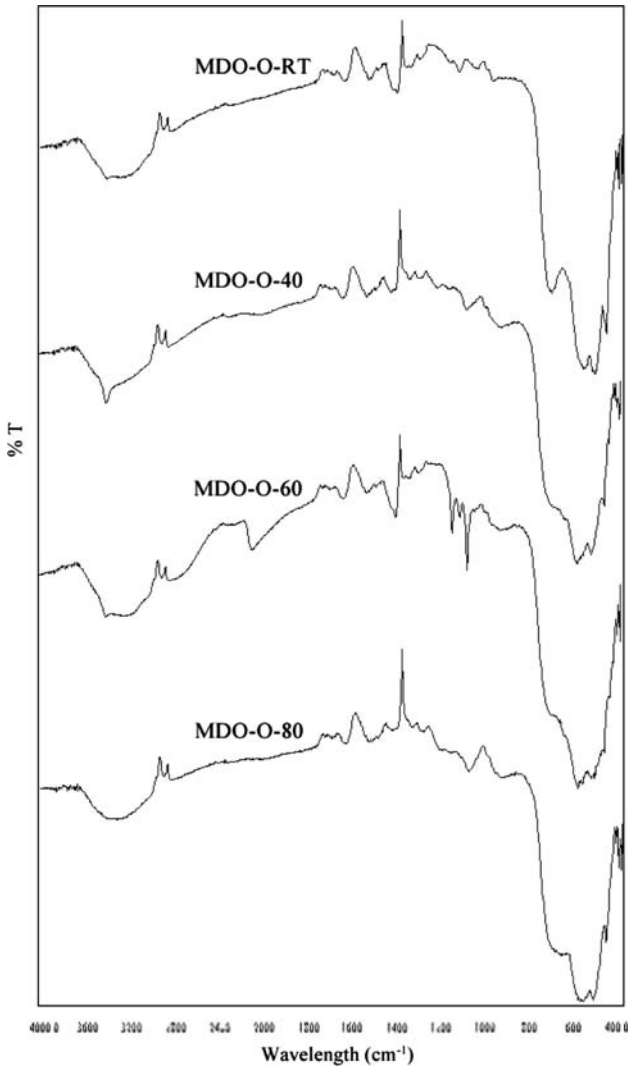

Fig. 3 FTIR spectra of MnO_2 samples prepared at different temperatures

comprising of four different stages [24]. The first stage is from room temperature up to 110 °C represents physically bonded water and the second stage is from 110 to 400 °C and represents chemically bonded water. The weight loss in

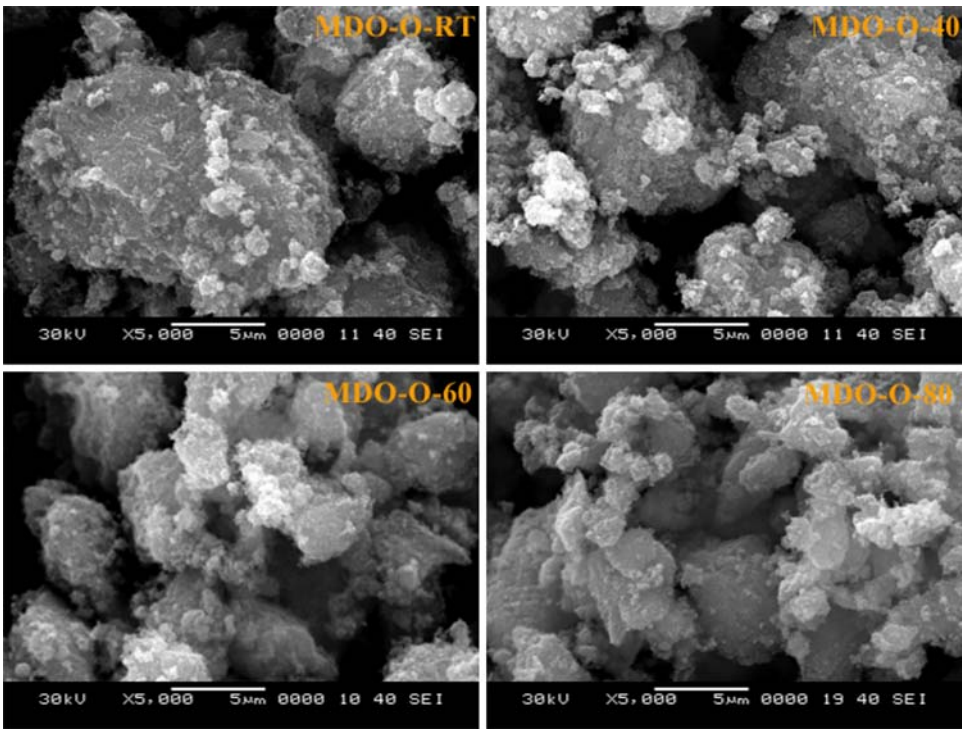

Fig. 4 SEM images of the prepared MnO_2 samples

the temperature range 150 to 400 °C, the weight loss represents the removal of structural water [25, 26]. All the structural water present in the form of OH ions is associated with either Mn^{4+} vacancies (x) or Mn^{3+} (y) in the network of MnO_2. Removal of this structural water while heating causes healing out of cation vacancies and the oxidation of Mn^{3+}–Mn^{4+}. Thereby, Mn cations jump into vacant lattice positions and protons associated with vacancies diffuse to the surface of the crystal, where they combine with surplus O^{2-} to form water, which then evaporates [10]. The third stage weight loss occur in the range 400–600 °C, which is due to the formation of Mn_2O_3 and the last stage weight loss i.e. from 600 to 800 °C represents the transformation from Mn_2O_3 to Mn_3O_4 [27, 28]. The percentage weight loss over different temperature ranges is listed in Table 2. The weight loss over different temperature ranges is consistent for all samples except MDO-O-40.

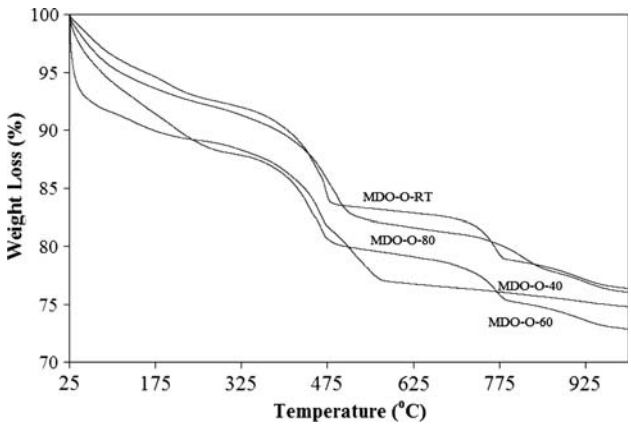

Fig. 5 TG curves of MnO_2 samples prepared at different temperatures

Figure 6 presents DTA curves of the prepared samples. MDO-O-60 and MDO-O-80 show broad endotherms corresponding to structural water removal. All samples exhibit endothermic peak ~480 °C corresponding to the thermal decomposition reaction $MnO_2 \rightarrow Mn_2O_3$ [29]. An additional shoulder-like endothermic peak at ~460 °C corresponds to the decomposition of MnO_2 to Mn_5O_8 and Mn_2O_3 [30] according to the reaction:

$$7MnO_2 \rightarrow Mn_5O_8 + Mn_2O_3 + 1.5O_2 \quad (1)$$

Further heating results in the decomposition of Mn_2O_3 to Mn_3O_4 at ~800 °C. Slight shift in the temperature can

Table 2 TG data of the synthesized MnO_2

Sample code	Percentage weight loss for temperature range (°C)				
	40–110	110–300	300–400	400–600	600–1000
MDO-O-RT	2.96	4.17	1.97	8.30	7.64
MDO-O-40	3.64	2.98	1.99	11.62	2.74
MDO-O-60	4.33	6.32	1.80	8.31	8.14
MDO-O-80	3.17	3.88	2.26	8.74	7.02

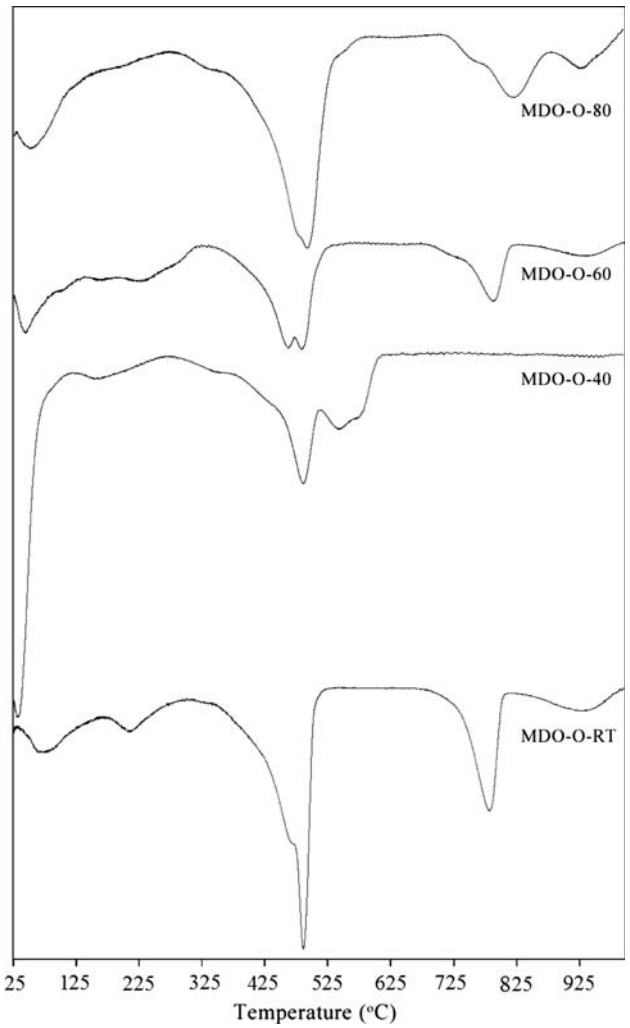

Fig. 6 DTA curves of MnO_2 samples prepared at different temperatures

be attributed to the experimental variations such as particle size, crystallite size, and porosity etc. [31].

3.5 Chemical composition and formulae

The results of chemical analyses are depicted in Table 3. The high percentage of available oxygen in all cases indicates that prepared samples can be used as cathode materials for of high drain discharge cell. Based on chemical composition data, the formulae are expressed in the format proposed by Brenet [32] which is as follows:

$$(MnO_2)_{2n-3}\cdot(MnOOH)_{4-2n}\cdot mH_2O \quad (2)$$

where the number of neutral water molecules m in the crystal lattice was calculated from the percentage of combined water (y), using the relation:

$$m = \frac{91y + 2n(900 - y) - 3600}{18(100 - y)} \quad (3)$$

where y is the percentage of the combined water, determined from weight loss occurred during TG between temperature 25 and 300 °C. Fraction of Mn^{3+} ions 'n' is determined by the relation:

$$n = \frac{3 + x}{2} \quad (4)$$

where x in MnO_{1+x} is the ratio of reducible Mn to the total Mn and is calculated using the relation:

$$x = \frac{0.632 \times \%MnO_2}{\%Mn} \quad (5)$$

Ruetschi proposed a cation vacancy model [10] to explain the physical and electrochemical properties of 'γ- and ε-manganese dioxides. Accordingly, the general formulae of active manganese dioxides, i.e. $(MnO_2)_{2n-3}(MnOOH)_{4-2n}\cdot mH_2O$ can be represented by:

$$Mn_{(1-x-y)}{}^{4+}\cdot Mn_y{}^{3+}\cdot O_{(2-4x-y)}{}^{2+}\cdot OH_{(4x+y)}{}^{1-} \quad (6)$$

where x is the fraction of Mn^{4+} missing from the MnO_2 lattice resulting in Mn vacancies; y is the fraction of Mn^{4+} replaced by Mn^{3+}. The parameters 'x' and 'y' in the above equation are related to the Brenet's parameters 'n' and 'm'. The relation between Brenet's formula and Ruetschi's formula is as follows:

$$x = \frac{m}{2 + m} \quad (7)$$

$$y = \frac{4(2 - n)}{2 + m} \quad (8)$$

Ruetschi's model could briefly be summarized as follows. The γ/ε-MnO_2 lattice is composed of O^{2-}, OH^{1-}, Mn^{4+}, Mn^{3+}, and □ vacancies. The structural water, which is present, is associated with □ vacancies or Mn^{3+} ions.

Table 3 Chemical composition, reactivity and formulae of the prepared manganese dioxides samples

Sample code	MnO_2 (%)	Mn (%)	x in $MnO_{(1+x)}$	Combined water (y) (%)	Neutral water molecules (m)	Fraction of Mn^{3+} ions (n)	Formula $(MnO_2)_{(2n-3)}\cdot(MnOOH)_{(4-2n)}\cdot mH_2O$
MDO-O-RT	90.78	60.33	0.95	7.64	0.373	1.976	$(MnO_2)_{0.951}\cdot(MnOOH)_{0.049}\cdot 0.372H_2O$
MDO-O-40	86.65	61.07	0.90	11.18	0.549	1.948	$(MnO_2)_{0.897}\cdot(MnOOH)_{0.103}\cdot 0.548H_2O$
MDO-O-60	83.99	61.38	0.86	11.84	0.572	1.933	$(MnO_2)_{0.865}\cdot(MnOOH)_{0.135}\cdot 0.572H_2O$
MDO-O-80	90.75	61.10	0.94	8.30	0.404	1.970	$(MnO_2)_{0.939}\cdot(MnOOH)_{0.061}\cdot 0.404H_2O$

Neither the vacancy nor the proton associated with Mn^{3+} is mobile. The protons, however, can execute jumps to adjacent O^{2-} ions under the influence of fresh protons when Mn^{4+} ions are being reduced to Mn^{3+}. Surface chemisorbed water is present in the form of OH^{1-} groups. The surface is presumed to consist of a 'continuous layer of Mn^{4+} vacancies'. Two surface vacancies are equivalent to one interior vacancy. Based on these postulate Ruetschi recommended the above formula for γ/ε-MnO_2. For the prepared samples, the vacancy fraction value varies from 0.157 to 0.222 in MDO-O-RT and MDO-O-60, respectively (Table 4). Consequently, the y value of Ruetschi which represents Mn^{3+} in MnO_2 is found to vary between 0.041 to 0.105 in MDO-O-RT and MDO-O-60, respectively.

This model explains several physical properties of manganese dioxides such as density, structural water content, proton transfer rate, theoretical maximum electrochemical capacity, etc.

The density was calculated using the relationship

$$d = \frac{54.94(1-x) + 32 + 1.008(4x)}{V_o} \quad (9)$$

where x is cation vacancy fraction and V_o unit cell volume for γ-MnO_2 ($V_o = 17.805$ cm^3). Introduction of vacancies into the Mn^{4+} sublattice, and associated substitutions of $4O^{2-}$ by $4OH^-$, does not lead to a noticeable change in lattice parameters. However, owing to loss of Mn^{4+} ions due to the formation of vacancies, the density decreases with increasing vacancy fraction. The above expression is plotted in Fig. 7 for $y = 0$. The results obtained are in accordance with the model.

The total structural water content is expressed by the formula:

$$\%H_2O = \frac{100 \times [18.016(4x + y)]}{2MW} \quad (10)$$

where MW is the molecular weight calculated using Eq. 6. The structural water content (%) for the cases $y = 0$ and $y = 0.1$ is plotted, as a function of cation vacancy 'x' in Fig. 8. The linear relationship between structural water and cation vacancy is in agreement with Ruetschi's model. The values are comparable with that calculated from weight-loss in thermal studies. Combining results of Figs. 7 and 8,

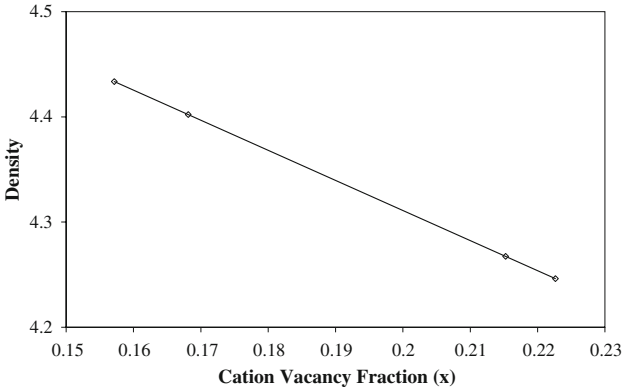

Fig. 7 Density (gm cm^{-3}) as a function of Mn^{4+} vacancy fraction (x)

the theoretical relationship between structural water and density is experimentally verified. It is seen that density decreases with increasing structural water content (Fig. 9).

The theoretical (maximum) electrochemical capacity deliverable per unit weight (C_w) was calculated as follows [10]:

$$C_w = \frac{(1-x-y)26.8}{MW}(\text{Ah g}^{-1}) \quad (11)$$

where 26.8 in the theoretical mA h [11]. From C_w values, percentage theoretical electrochemical capacity ($\%C_w$) was calculated using the relation:

$$\%C_w = \frac{C_w \times 100}{0.308} \quad (12)$$

where 30.8 is the theoretical output of pure MnO_2 [10] (*Note*: $x = 0$ and $y = 0$; for pure MnO_2). The calculated values are plotted for $y = 0$ as a function of x in Fig. 10. It demonstrates how theoretical maximum capacity decreases with increasing vacancy fraction i.e. with increasing water content. Thus, high percentage of structural water is undesirable for as regards to capacity. However, certain amount of it is necessary for a fast proton transfer rate for effective electrochemical activity.

3.6 Electrochemical activity

Electrochemically, the quantity of electricity generated on constant load to a certain end-voltage determines relative activity. It not only depends on the quality of MnO_2, but

Table 4 Correlation of physical and electrochemical properties of the prepared manganese dioxides samples

Sample code	x (Ruetschi)	y (Ruetschi)	Mol. Wt. (g)	Density (g cm^{-3})	% H_2O for $y = 0$ (Ruetschi)	C_w (Ah g^{-1})	C_w (%)	Formula $Mn_{(1-x-y)}{}^{4+}\cdot Mn_y{}^{3+}\cdot O_{(2-4x-y)}{}^{2-}\cdot OH_{(4x+y)}{}^{1-}$
MDO-O-RT	0.157	0.041	78.97	4.434	7.171	0.272	88.33	$Mn_{0.801}{}^{4+}\cdot Mn_{0.041}{}^{3+}\cdot O_{1.330}{}^{2-}\cdot OH_{0.669}{}^{1-}$
MDO-O-40	0.215	0.081	76.05	4.268	10.199	0.248	80.51	$Mn_{0.703}{}^{4+}\cdot Mn_{0.081}{}^{3+}\cdot O_{1.057}{}^{2-}\cdot OH_{0.942}{}^{1-}$
MDO-O-60	0.223	0.105	75.70	4.246	10.598	0.238	77.28	$Mn_{0.672}{}^{4+}\cdot Mn_{0.105}{}^{3+}\cdot O_{1.004}{}^{2-}\cdot OH_{0.995}{}^{1-}$
MDO-O-80	0.168	0.051	78.42	4.402	7.725	0.266	86.64	$Mn_{0.780}{}^{4+}\cdot Mn_{0.051}{}^{3+}\cdot O_{1.276}{}^{2-}\cdot OH_{0.723}{}^{1-}$

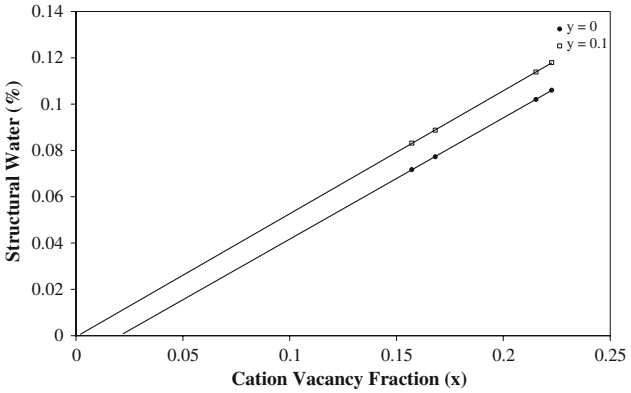

Fig. 8 Structural water content as a function of Mn^{4+} vacancy fraction (x)

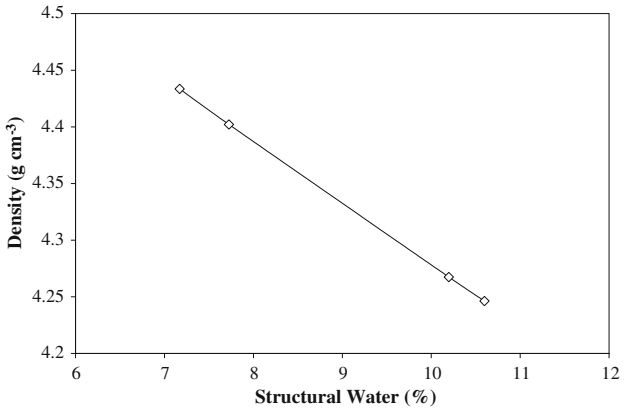

Fig. 9 Density as a function of structural water content

also on the structural and dimensional features of the cathode [33]. In this context, differences in the electrochemical reactivity of manganese dioxides can be easily recognized by discharging them in 9 M KOH solution. Since this method has added advantage of supposedly being independent of cell fabrication factors [34], it has been adopted in the present work.

Figures 11 and 12 presents discharge curves for the prepared samples in 9 M KOH at 1 mA 0.1 g^{-1} and 100 Ω 0.5 g^{-1}, respectively. The corresponding discharge parameters are summarized in Tables 5 and 6, respectively. At low current regime, MnO_2 is reduced in two steps (Fig. 11); whereas at high current regime, the second step becomes less clear (Fig. 12). During the first step i.e. from MnO_2 to $MnO_{1.5}$, the voltage decreases continuously, producing an S-shaped curve. This stage is accompanied by simultaneous insertion of protons and electrons into the ionic crystal of MnO_2. The concentration of Mn^{3+} and OH^- ions in the lattice increases gradually, and MnO_2 is converted to MnOOH according to the reaction:

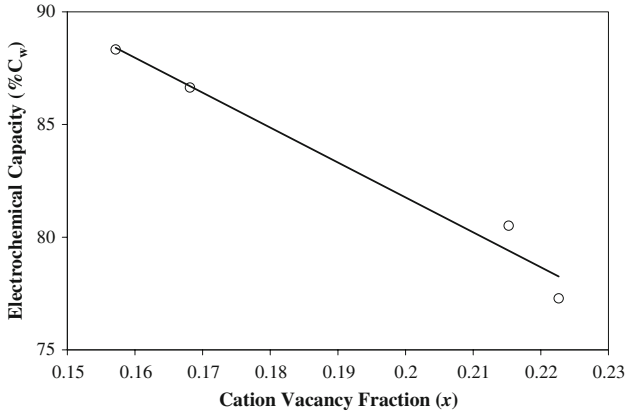

Fig. 10 Theoretical electrochemical capacity per unit weight, as a function of Mn^{4+} vacancy fraction (x) for $y = 0$ (undischarged states)

$$MnO_2 + H^+ + e^- \rightarrow MnOOH \quad (13)$$

The conversion takes place without any major change in basic structure of host MnO_2 and hence, the process is homogeneous-phase reduction. The second step is from $MnO_{1.5}$ to $MnO_{1.0}$, wherein the potential remains almost constant during the major portion of the step. This step consists of the following three consecutive stages: (i) dissolution of MnOOH (Mn^{3+}) in form of complex ions such as $[Mn(OH)_4]^-$ into the electrolyte, (ii) reduction of $[Mn(OH)_4]^-$ to $[Mn(OH)_4]^{2-}$ and (iii) precipitation of $Mn(OH)_2$ from saturated solution of $[Mn(OH)_4]^{2-}$. The complete process is heterogeneous-phase reaction [35].

The sloping nature of discharge curve i.e. continuous decay of voltage, during step 1, is due to the solid-state one-electron reduction process according to Eq. 13. Since the process involves the introduction of protons into the crystal

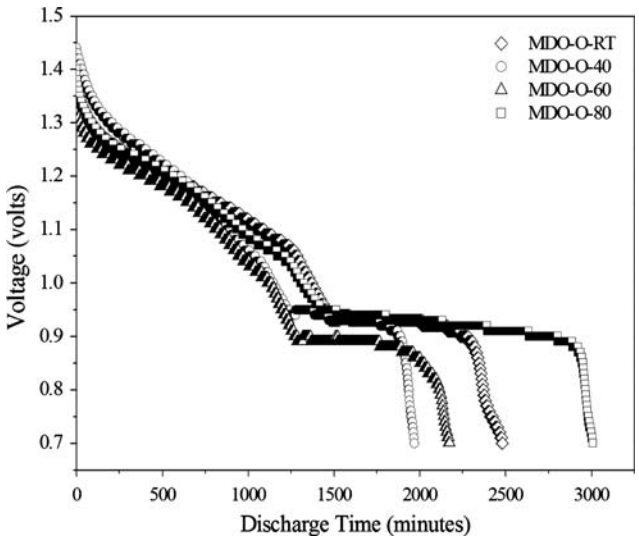

Fig. 11 Discharge curves of the prepared samples in 9 M KOH at constant current (1 mA 0.1 g^{-1})

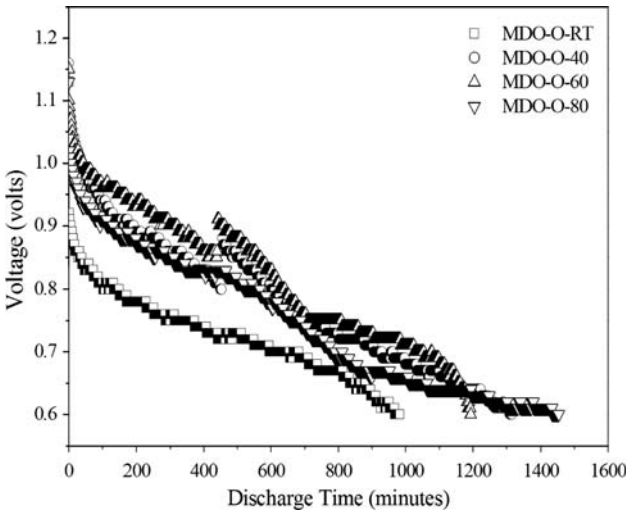

Fig. 12 Discharge curves of the prepared samples in 9 M KOH at constant resistance (100 Ω 0.5 g^{-1})

lattice, it occurs in a single phase whereby lattice expands with increasing degree of reduction. The OH^- ions, which are incorporated into the lattice as a consequence of Mn^{4+} cation vacancies, acts as proton donors providing initial concentration of protons for Eq. 13. The probability of proton transfer is expressed as:

$$P_t = v[OH][O^{2-}] \tag{14}$$

where v is the jump frequency, $[OH^-]$ represents concentration of proton occupied sites and $[O^{2-}]$ the concentrations of available, suitable empty sites for proton transfer. If these concentration terms are expressed as number of ions per molecular volume i.e. in terms of Ruetschi's model

$$P_t = v[4x + y][2 - 4x - y] \tag{15}$$

In γ-MnO_2, two types of $[O^{2-}]$ and $[OH^-]$ sites can be distinguished: the planar $[O^{2-}]_{pl}$, $[OH^-]_{pl}$ and the pyramidal $[O^{2-}]_p$, $[OH^-]_p$ configuration with respect to the three next-neighbouring Mn^{4+} ions. Only the 'pyramidal' O^{2-} are suitable sites for proton uptake [36]. Thus, the rate of proton transfer (P_t) in the γ-MnO_2 could be visualized as being proportional to:

$$\begin{aligned} P_t &= v[OH]_{pl}\cdot[OH]_p\cdot[O^{2-}]_p \\ &= (4-p)x\cdot(px+y)\cdot(1-px-y) \end{aligned} \tag{16}$$

This expression is plotted in Fig. 13 as a function of x, for $p = 2$, and for several values of y as parameter. Accordingly, for small values of x and y, the rate of proton transfer increases with the cation vacancy fraction x and OH^- concentration y. x values greater than 0.25 could be detrimental. They would correspond to very high structural water contents [10, 12], and would produce lower electrochemical activity.

The values of x for the prepared samples are in the range $0.15 < x < 0.22$ i.e. within the specified range of $x < 0.25$. However, energy density has decreased after $x = 0.17$ (Fig. 14), contradicting to Ruetschi's model. The energy density of the prepared samples increases in order MDO-O-80 < MDO-O-RT < MDO-O-60 < MDO-O-40 (Table 4). The lower energy density of MDO-O-40 and MDO-O-60 can be explained on the basis of high structural water

Table 5 Discharge characteristics of MnO_2 samples in 9 M KOH at constant current 1 mA 0.1 g^{-1}

Sample code	Open circuit voltage (V)	Discharge time to 0.9 V cutoff (min)	Discharge capacity (mA h 0.1 g^{-1})	Gravimetric energy density (W h kg^{-1})[a]	Volumetric energy density (W h L^{-1})[a]
MDO-O-RT	1.431	2280	41.38	104.25	256.80
MDO-O-40	1.487	1883	32.80	84.98	209.34
MDO-O-60	1.437	1359	36.23	88.73	218.57
MDO-O-80	1.428	2806	50.12	123.23	303.56

All calculations for 100 mg MnO_2 sample

[a] Cutoff 0.7 V; based on obtained average operating voltage per cell

Table 6 Discharge characteristics of MnO_2 samples in 9 M KOH at constant resistance 100 Ω 0.5 g^{-1}

Sample code	Open circuit voltage (V)	Discharge time to 0.6 V cutoff (min)	Discharge capacity (mA h 0.5 g^{-1})	Gravimetric energy density (W h kg^{-1})[a]	Volumetric energy density (W h L^{-1})[a]
MDO-O-RT	1.471	982	116.95	40.59	99.99
MDO-O-40	1.531	1315	168.60	62.88	154.90
MDO-O-60	1.465	1192	161.07	63.22	155.74
MDO-O-80	1.477	1453	177.79	63.31	155.96

All calculations for 500 mg MnO_2 sample

[a] Cutoff 0.6 V; based on obtained average operating voltage per cell

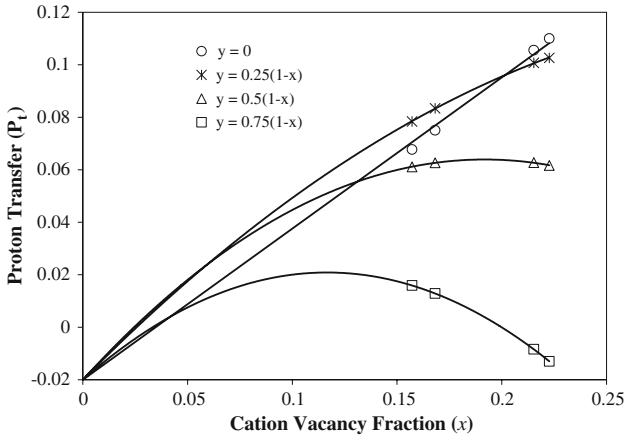

Fig. 13 Relative proton transfer rate (P_t) as a function of Mn^{4+} vacancy fraction

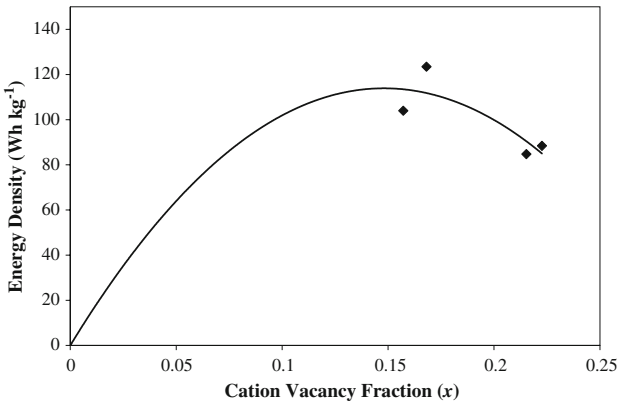

Fig. 14 Energy density as a function of Mn^{4+} vacancy fraction

content (11.42 and 11.82%, respectively) and high values of y content (0.041 and 0.081, respectively). The y value, which signifies Mn^{3+} content in the sample [7], results in decreased electrochemical performance due to the formation of electrochemically inactive Mn(III) intermediate [13] during the discharge process. MDO-O-RT and MDO-O-80, on the other hand, show low values of combined water content and y content (Tables 3 and 4), thereby showing higher energy density as compared to other samples. Thus, the cation vacancy fraction (x) and structural water content and Mn^{3+} content (y) determines the electrochemical activity for the prepared samples [37].

3.7 Cyclic voltammetry

Figure 15 shows the cyclic voltammogram of MDO-O-80 in potential range −800 to 300 mV for first four cycles. As described in earlier section, reduction of MnO_2 in 9 M KOH takes place in two steps. In voltammogram, homogeneous phase reduction shown by Eq. 13 takes place in the potential region 200 to −300 mV. Upon cycling to

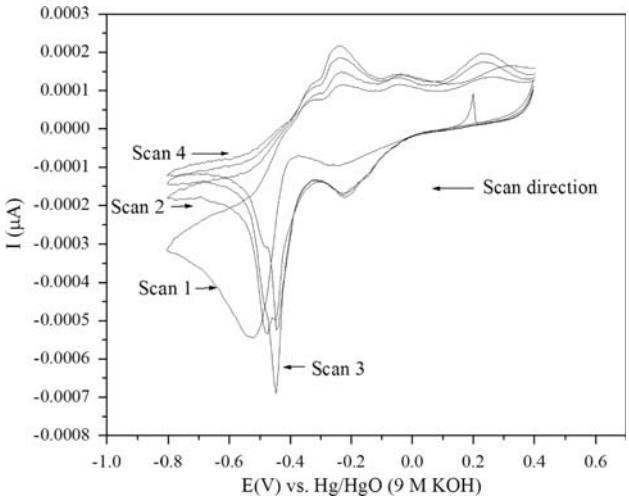

Fig. 15 Cyclic voltammogram of MDO-O-80 in 9 M KOH. Hg/HgO/9 M KOH reference electrode, scan rate 2 mV s^{-1}

more negative potentials i.e. from −300 to −800 mV, heterogeneous phase reduction of MnOOH to $Mn(OH)_2$ is observed through a well-defined peak(s) in region −400 mV to −500 mV [17, 38, 39]. During oxidation cycles, Mn(III) species are regenerated in region −300 to 0 mV, whereas the peak at 300 mV is due to the formation of δ-MnO_2 from $Mn(OH)_2$ [17, 38–40]. The shape and peak potentials of cyclic voltammograms recorded agree with data of composite electrodes recorded at 25 μV s^{-1} [38], at 2 mV s^{-1} [17, 39] and at 25 mV s^{-1} [40].

4 Conclusions

Chemical manganese dioxides containing structural disorder were prepared using industrial grade manganese sulfate. The merging of lines such as h21/h40 and h02/h61 in the XRD patterns suggested heavy microtwinning defect ($T_w > 70\%$), whereas the de Wolff disorder (P_r) was found to increase with the reaction temperature. During discharge process in 9 M KOH, the OH^- associated with Mn^{4+} cation vacancy acted as a proton donor in the first stage of process. The rate of proton transfer during this stage was proportional to the Mn^{4+} cation vacancy fraction. However, the energy density dropped with the increasing vacancy fraction, which was attributed to the high amount of structural water content and Mn(III) content associated with the corresponding samples.

References

1. Donne SW, Kennedy JH (2004) J Appl Electrochem 34:159

2. Ufer A, Lawrence GA, Swinkles DAJ (1997) J Appl Electrochem 27:667
3. Prélot B, Poinsignon C, Thomas F, Schouller E, Villiéras F (2003) J Colloid Interface Sci 257:77
4. de Wolff PM (1959) Acta Cryst 12:51
5. Pannetier J (1992) Batteries Battery Mater 11:51
6. Chabre Y, Pannetier J (1995) Prog Solid State Chem 23:1
7. Abbas H, Abou-El-Sherbini Kh, Askar M (2001) J Mater Sci Technol 17(3):351
8. Sasaki K, Kozawa A (1957) J Electrochem Soc Jpn 25:115
9. Coeffier G, Brenet JP (1965) Electrochimica Acta 10:1013
10. Ruetschi P (1984) J Electrochem Soc 131:2737
11. Desai BD, Dhume RAS, Dalal VNK (1988) J Appl Electrochem 18:62
12. Fernandes JB, Desai BD (1991) J Power Sources 34:207
13. Abbas H, Nasser SA (1996) J Power Sources 58:15
14. Abou-El-Sherbini KhS (2002) J Solid State Chem 166:375
15. Vogel AI (1989) A textbook of Quantitative Inorganic Analysis 5th edn, Addison Wesley Lognmans Inc., London, 336 pp
16. Indian Standard, Manganese dioxide for dry batteries, IS-11153 (1984)
17. Fiedler DA (1998) J Solid State Chem 2:315
18. de Wolff P, Visser JW, Giovanoli R, Brutsch R (1978) Chimia 32:257
19. Simon DE, Morton RW, Gislason JJ (2004) Adv X-ray Anal 47:267
20. Kim C-H, Akase Z, Zhang L, Heuer AH, Newman AE, Hughes PJ (2006) J Solid State Chem 179:753
21. Fernandes JB, Desai BD, Dalal VNK (1983) Electrochim Acta 28:309
22. Ananth MV, Pethkar S, Dakshinamurthi K (1998) J Power Sources 75:278
23. Potter RM, Rossman GR (1979) Am Mineral 64:1199
24. Ohzuku T, Tari I, Hirai T (1982) Electrochim Acta 27:1049
25. Ruetschi P, Giovanoli R (1988) J Electrochem Soc 35:2663
26. Lee JA, Newnham CE, Stone FS, Tye FL (1973) J Colloid Interface Sci 45:289
27. Sharp JH, Tinsley DM (1971) J Therm Anal 3:43
28. Fernandes JB, Desai BD, Dalal VNK (1985) J Power Sources 16:1
29. Zaki MI, Hasan MA, Pasupulety L, Kumari K (1997) Thermochim Acta 303:171
30. Liu B, Thomas PS, Ray AS, Williams RP (2004) J Therm Anal Calorim 76:115
31. Gonzalez C, Gutierrez JI, Gonzales-Velasco JR, Cid A, Arranz A, Arranz JF (1998) J Therm Anal Calorim 52:985
32. Brenet JP, Cyrankowsa M, Ritzler G, Saka, R, Traore K (1975) Proceedings of MnO_2 Symposium, Cleveland, OH, USA, vol 1, p 276
33. Balewski L, Brenet JP (1967) Electrochem Technol 5(11–12):527
34. Kozawa A (1979) Prog Batt Sol Cells 2:104
35. Kozawa A, Kordesch K (eds) (1974) Batteries vol 1 manganese dioxide, Marcel Dekker, Inc. New York, 389 pp
36. Maskell WC, Shaw IE, Tye FL (1983) Electrochim Acta 28:225
37. Malankar HY, Umare SS, Singh K, Sharma M (2009) J Solid State Electrochem. doi:10.1007/s10008-009-0790-9
38. McBreen J (1975) Electrochim Acta 20:221
39. Fiedler DA, Besenhard JO, Fooken MH (1997) J Power Sources 69:157
40. Ghaemi M, Gholami A, Moghaddam RB (2008) Electrochim Acta 53:3250